

Full length article

In-situ neutron diffraction during biaxial deformation



S. Van Petegem^a, J. Wagner^{a,1}, T. Panzner^c, M.V. Upadhyay^a, T.T.T. Trang^{a,b},
H. Van Swygenhoven^{a,b,*}

^a Swiss Light Source, Paul Scherrer Institut, CH-5232 Villigen PSI, Switzerland

^b Neutrons and X-rays for Mechanics of Materials, IMX, École Polytechnique Fédérale de Lausanne, CH-1012 Lausanne, Switzerland

^c Laboratory for Neutron Scattering, NUM, Paul Scherrer Institut, CH-5232 Villigen PSI, Switzerland

ARTICLE INFO

Article history:

Received 6 October 2015

Received in revised form

23 November 2015

Accepted 3 December 2015

Available online 9 January 2016

Keywords:

Mechanical testing

In situ neutron diffraction

Strain path changes

Biaxial

ABSTRACT

A change in strain path may have a significant effect on the mechanical response of metals. In order to understand or even predict the macroscopic behaviour under such conditions a detailed knowledge on the microstructural evolution is crucial. Yet relatively little work has been done to quantify and understand how the inter- and intragranular strains are affected during a change in strain path. In this work we present a new multiaxial deformation rig that allows performing in situ proportional and non-proportional loading under neutron diffraction. We demonstrate the capabilities of this new setup for the case of a 316 L stainless steel. We show that the nature and magnitude of intergranular strain strongly depends on the applied stress state and demonstrate that micro yielding and internal strain recovery are responsible for the observed transient softening during a 90° strain path change. We anticipate that this new characterization method will provide previously inaccessible microstructural data that can serve as input for benchmarking current state-of-the-art crystal plasticity models.

© 2015 Acta Materialia Inc. Published by Elsevier Ltd. This is an open access article under the CC BY-NC-ND license (<http://creativecommons.org/licenses/by-nc-nd/4.0/>).

1. Introduction

Engineering materials often experience complex strain paths during synthesis or under service conditions. A prime example is metal forming, which typically involves multiple operations including strain path changes during which transient and permanent changes in hardening rate are observed (see, for instance [1], and references therein). Many metals exhibit a lower yield stress (Bauschinger effect [2]) when the sign of the load is reversed after plastic deformation, in spite the hardening observed during the forward straining path. Some materials however exhibit a larger yield stress after the loading direction is changed, a phenomenon called cross-effect [3]. Furthermore, softening/hardening upon changing strain path can be a transient phenomenon or permanent where differences in hardening rate between the first and the second loading path maintain. These phenomena play an important role in manufacturing and have to be taken into account when setting forming limits.

The origin of such strain path dependence has to be found at the inter- and intra-granular level. Polycrystalline metals yield heterogeneously and this leads to inter-granular stresses, which remain after unloading and will have to be added to the stress applied in the next strain path. Dislocation slip, an inherent anisotropic mechanism, will develop anisotropic dislocation substructures within the individual grains, generating long range intragranular stresses that will have to be considered simultaneously with the intergranular stresses [4]. Incorporation of the above effects on the correct physical length scale through multi-scale modelling can offer significant improvements in computer-aided engineering. Modelling non-monotonous and/or non-proportional deformation requires improved constitutive equations [1,5,6]. Different models have been put forward to incorporate for instance the Bauschinger effect [7]. These computational models necessarily need to take into account the evolution of the microstructure and in particular the development of internal stresses.

In the last decade in-situ x-ray and neutron diffraction has been extensively used to investigate the evolution of intergranular and intragranular stresses during deformation. The information has been directly compared with various crystal plasticity models [8–12]. Most studies are however restricted to uniaxial tension or compression tests. Some in-situ strain path change experiments

* Corresponding author. Villigen, Villigen-PSI, Switzerland.

E-mail address: helena.vs@psi.ch (H. Van Swygenhoven).

¹ Now at KNMF, Karlsruhe Institute of Technology, D-76344 Eggenstein Leopoldshafen, Germany.

have been performed, in particular tension-compression Bau-schinger tests [13–15]. In 2013 Repper et al. [16] have performed the first in-situ neutron diffraction study on cruciform shaped specimen. They have demonstrated that during equibiaxial loading the evolution of lattice strain is quite different from that during uniaxial straining. Foecke et al. have implemented various devices inside a large laboratory x-ray diffractometer in order to measure multiaxial stress–strain curves and corresponding yield loci [17–19]. Here diffraction is used to obtain the macroscopic stress state in the sample using the $\sin^2\psi$ method. Imbeni et al. [20] have performed in situ tension and torsion experiments on thin tubular samples of Nitinol during X-ray diffraction. Mehta and coworkers [21] used X-ray microdiffraction to map out multiaxial strain fields in Nitinol.

Recently it was shown that in case of a 90° strain path change the commonly used models fail to predict both the magnitude and nature of intergranular stresses that arise as a consequence of elastic and plastic anisotropy [22]. In order to further optimize crystal plasticity models there is a clear need for adequate in-situ devices allowing studies of engineering materials subjected to complex strain paths. Collins and co-workers [23] have developed a new setup to perform in-situ x-ray diffraction during biaxial deformation of sheets. They have studied the evolution of lattice strain and texture during uniaxial and biaxial tensile deformation of a cold rolled low carbon ferritic steel. It was shown that the distribution of lattice strain with respect to azimuthal angle is highly dependent on the applied biaxial strain ratio. Furthermore it was demonstrated that for strain ratios close to balanced biaxial the lattice strain initially accumulates more rapidly in the direction of the tensile axis with highest load, whereas at larger plastic strain the distribution becomes more uniform.

High-resolution reciprocal space mapping with high energy x-rays is a powerful method to investigate in detail the microstructural evolution during a strain path change. This has been demonstrated extensively for the case of Cu [4,24–26]. Wejdemann et al. have [4] demonstrated that during an orthogonal strain path change two different regimes can be distinguished: a microplastic regime during which the elastic stresses are significantly altered and only subgrain plasticity occurs, and a macroplastic regime where a new microstructure is formed. Unfortunately such measurements are rather time-consuming.

Some x-ray and neutron beam lines are now equipped with load frames that allow in-situ mechanical testing under multiaxial stress state and/or to perform strain path changes. At the DIFFABS beam line (SOLEIL, France) a biaxial deformation rig has been installed, which allows for in situ characterisation of thin polycrystalline films deposited on a compliant substrate [27,28]. At the engineering neutron diffractometer VULCAN (SNS, USA) a large load frame has been installed which allows for combined tensile/compression/torsion experiments [29,30].

In this work we present a unique biaxial deformation rig that can be used for in-situ biaxial proportional and non-proportional testing during neutron diffraction at the beamline POLDI of the Swiss Neutron Spallation Source (SINQ). The rig exhibits two independent axes and a torsional unit, which allows to apply various multiaxial stress states and to perform complex strain path changes. We apply this method to study the evolution of the inter/intra granular stresses in a 316 L stainless steel known to exhibit transient softening when changing the strain path [22]. We show that the nature and magnitude of intergranular strain strongly depends on the applied stress state and demonstrate that micro yielding and internal strain recovery are responsible for the observed transient softening during a 90° strain path change. We anticipate that this new characterization method will provide previously inaccessible microstructural data that can serve as input

for benchmarking current state-of-the-art crystal plasticity models.

2. Material and methods

2.1. Multi-axial deformation rig

The in situ multi-axial deformation rig has been developed in collaboration with Zwick/Roell (Ulm, Germany) and is based on an innovative modular approach, which allows for testing under various complex deformation modes. Fig. 1 (in web version) displays a picture of the rig mounted on the 3D translation and rotation stage of the POLDI beam line. It consists of a 100 kN standard load frame that is equipped with a 200 Nm torsion unit, which allows for both regular tension/compression tests and proportional and non-proportional biaxial tension/torsion tests. Additionally a 50 kN axis can be mounted perpendicular to the main axis. With this setup in-plane proportional and non-proportional deformation tests on cruciform-shaped specimen can be performed. With these various possibilities the rig allows covering large part of the stress space. In what follows we will focus on the in-plane biaxial setup. The machine is controlled with testXpert, the standard control software from Zwick/Roell. In order to control the machine remotely, an interface between testXpert and SICS (SINQ Control System) has been written. This allows for full control of the deformation rig within the standard POLDI software environment.

2.2. Samples

The machine is designed for mounting planar cruciform shaped samples. Optimizing the shape of such samples is not a trivial task and has been topic of many studies (see, for instance, Refs [30–34]). Fig. 2 (left) displays a picture of the type of samples used in this work. The most important feature is the thickness reduction at the centre of the sample (from 10 mm in the arms to 3 mm in the gauge volume). The shape has been optimized with the aid of ABAQUS/Standard finite element modelling (FEM) [35]. Fig. 2 (right) shows the Von Mises stress distribution generated during equi-biaxial deformation. As expected stress concentrations occur at the notches, which results in local fracture at large levels of deformation. Therefore the value for the thickness reduction is a result of a trade-off between optimizing the volume for neutron diffraction and the possibility to reach at least 20% plastic strain in the centre, prior to fracture as the notches. For comparison regular flat dog-bone shaped specimen have been prepared. The gauge sections of these dogbones exhibit the same thickness as compared to the cruciform shaped samples. This ensures that the neutrons sample the same volume taken from the same section of the original material.

The material under investigation is a warm rolled 316 L stainless steel with composition 17.25Cr–12.81Ni–2.73Mo–0.86Mn–0.53Si–0.02C (wt%) purchased from ThyssenKrupp in a sheet thickness of 10 mm. The outer shape was cut using waterjet cutting whereas the thickness reduction is achieved by mechanical grinding. To learn more about the microstructure of the material corresponding with the region where the neutron diffraction data were collected, EBSD (electron back scatter diffraction) measurements were carried out at the center of the sheet plate (after etching away a 5 mm thick layer). Fig. 3 (left) shows a crystal orientation map of a representative area. The rolling and normal directions are indicated. The transvers rolling direction is perpendicular to the plane. As can be observed, the grains are equiaxed with an average grain size of 7 μm . On the right hand side of Fig. 3 the inverse pole figures for the three principal directions are shown. These show that there is no strong texture in the plane of the sheet. There are however more grains having a $\langle 001 \rangle$ or a $\langle 111 \rangle$ direction along the rolling

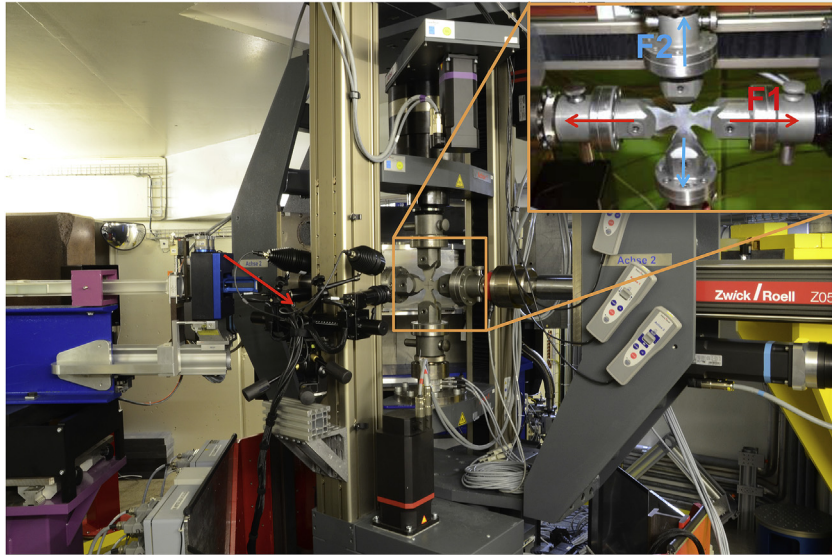


Fig. 1. Picture of the multi-axial deformation rig mounted at POLDI. The two-camera DIC system is marked by the red arrow. The inset shows in detail the cruciform sample together with the load axes F1 and F2. (For interpretation of the references to colour in this figure legend, the reader is referred to the web version of this article.)

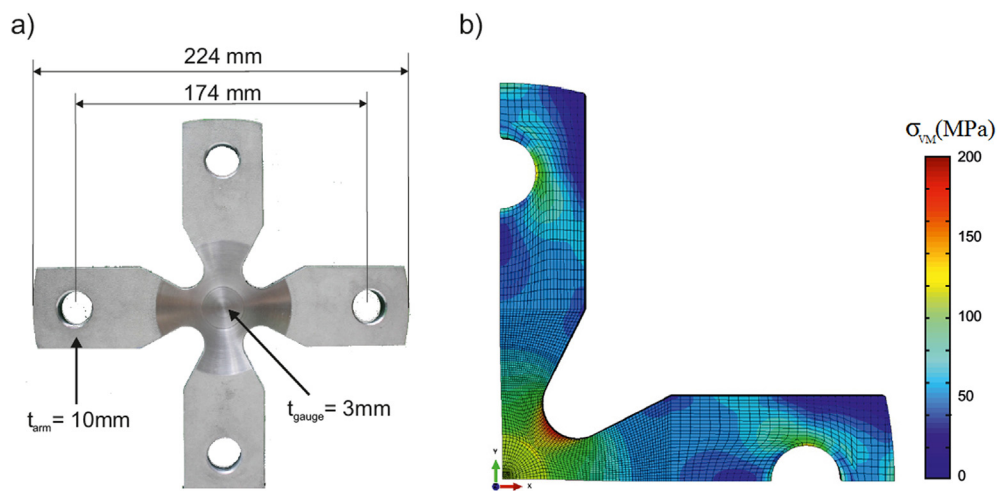


Fig. 2. (a) Image of the cruciform shaped specimen with dimensions indicated, (b) FEM simulation showing the von Mises stress distribution (in MPa) generated during equibiaxial to 23 kN in each arm. The ABAQUS/Standard simulations were performed on an 8th part of the cruciform geometry.

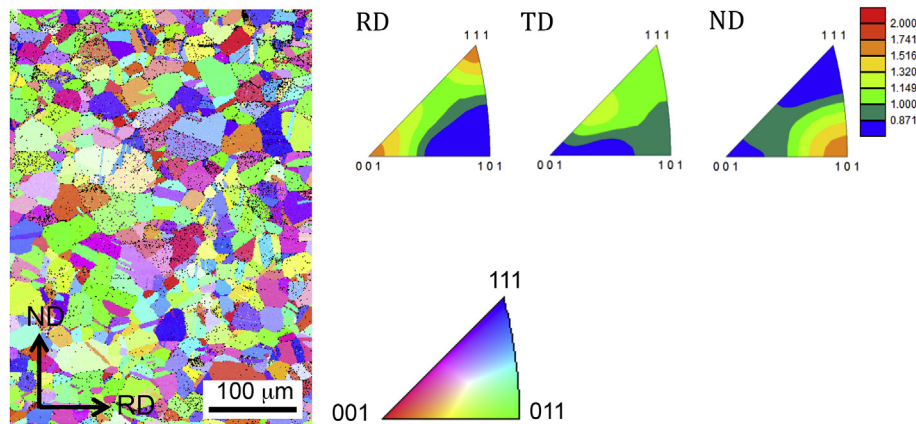


Fig. 3. (left) Orientation distribution map of a sample prior to deformation (right) inverse pole figures for the three principle directions: rolling (RD), transverse (TD) and normal (ND).

axis and a $\langle 101 \rangle$ along the normal direction. Relative to the other directions the ratio is of the order of 1.5, which means that the texture is mild.

2.3. Macroscopic strain measurements

The applied macroscopic strain is measured by a 3D digital image correlation system (GOM Aramis®). This is a full-field optical technique that provides high-resolution 2D or 3D displacements maps of the area of interest. The setup consists of two 5 MP CMOS cameras, both mounted at an angle of 15° to the normal of the centre of the cruciform sample. The field of view is typically about $20 \times 20 \text{ mm}^2$. A random speckle pattern is created on the sample by spraying fine paint droplets. Pair of images is acquired with a frequency of 1 Hz. With the Aramis analysis software the pairs of images are offline correlated with an initial set of images, resulting in 3D displacement maps. The macroscopic strain tensor is evaluated at the position where the neutron beam intersects with the sample. In this work a neutron beam of $3.8 \times 3.8 \text{ mm}^2$ has been used. This technique has the advantage that it allows (1) obtaining local strain information from the neutron gauge volume and (2) a quality assessment of the deformation test by checking the homogeneity of the displacement maps. Fig. 4 displays on the left the central part of a cruciform sample with the sprayed speckle pattern. On the right a macroscopic strain map after 21% plastic deformation as determined by the 3D-DIC system. The white rectangle represents the area where the neutron measurements are performed. Within this area the strain is quite uniform ($\pm 0.2\%$). The strain values reported in this work represent the average strain within this area.

From the macroscopic strain tensor ε we can derive the accumulated plastic strain:

$$\bar{\varepsilon}^p = \int \sqrt{\frac{2}{3}} d\varepsilon_{ij}^p d\varepsilon_{ij}^p \quad (1)$$

The von Mises stress is defined as:

$$\sigma_{vm} = \sqrt{\frac{3}{2}} \sigma_{ij}^d \sigma_{ij}^d \quad (2)$$

with σ^d the deviatoric stress tensor. Given the sample geometry it is safe to assume that we work under plane stress conditions. Furthermore the macroscopic strain tensor obtained from DIC indicates that shear stresses can be ignored for all tests discussed in

this work. Therefore equation (2) reduces to:

$$\sigma_{vm} = \sqrt{\sigma_{11}^2 - \sigma_{11}\sigma_{22} + \sigma_{22}^2} \quad (3)$$

with σ_{11} , σ_{22} the stress components along the principal axes 1 and 2. In case of equibiaxial loading equation (2) reduces to $\sigma_{vm} = \sigma_{11} = \sigma_{22}$.

2.4. In situ neutron diffraction

The neutron diffraction experiments are performed at POLDI, a time-of-flight (ToF) neutron strain scanner located at SINQ (Paul Scherrer Institut, Switzerland). Detailed information on the setup and principle can be found in Refs. [36,37]. Thanks to the ToF principle full diffraction patterns can be accumulated without having to move the sample or the detector. The diffraction geometry is shown in Fig. 5. The size of the incoming beam is determined by two pairs of slits with 3.8 mm opening. The gauge volume is further determined by a radial collimator, also with a 3.8 mm opening. The sample is positioned such that the scattering vector \mathbf{Q} lies in the plane of the sample. The inset of Fig. 5 displays the relationship between scattering vector and loading direction. When the sample is strained along axis F1 the loading direction is parallel to \mathbf{Q} . In contrast, when straining along axis F2 the loading direction is perpendicular to \mathbf{Q} .

The samples are strained with a fixed force rate of 40 N/s to prescribed force levels. In the elastic regime (both during loading and unloading) this force level is held constant during neutron accumulation. In the plastic regime the machine is stopped during neutron accumulation, in order to avoid extensive creep. During this period the stress relaxes slightly. Therefore, between reaching the prescribed force level and the actual neutron accumulation a wait period of 300s is included. Neutron diffraction spectra are then accumulated for 15min, during which the stress did not vary more than 10 MPa.

The data is analysed with the POLDI standard single peak fitting procedure implemented in Mantid [38]. The diffraction peaks are well described by Gaussian functions, yielding information on peak position, width and intensity. The peak position of each hkl -diffraction peak determines the mean interplanar lattice spacing d_{hkl} for the grain family with the hkl -direction parallel to the scattering vector \mathbf{Q} . The elastic lattice strain ε_{hkl} is then determined by the relative change of the interplanar lattice spacing d_{hkl} with respect to d_{hkl}^0 , the initial value prior to deformation:

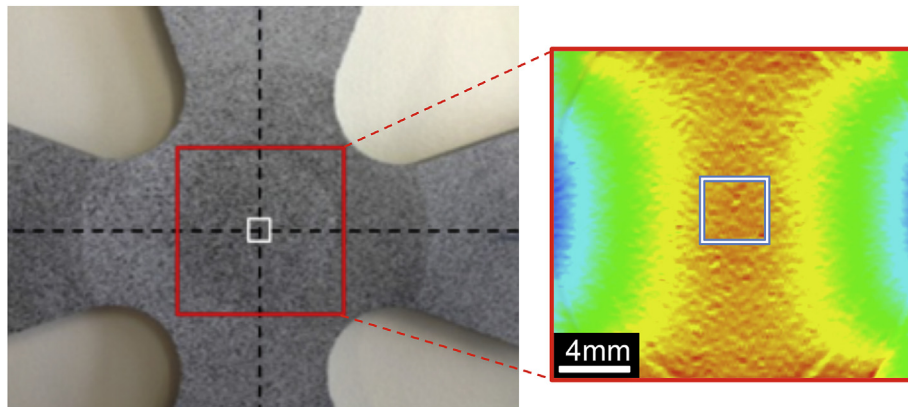


Fig. 4. Image of the centre of the cruciform shaped specimen with sprayed speckle pattern. The inset shows a map of the macroscopic strain component along the vertical axis at 21% plastic strain during a uniaxial test. The white rectangle represents the $3.8 \times 3.8 \text{ mm}^2$ area where the neutron measurements are performed.

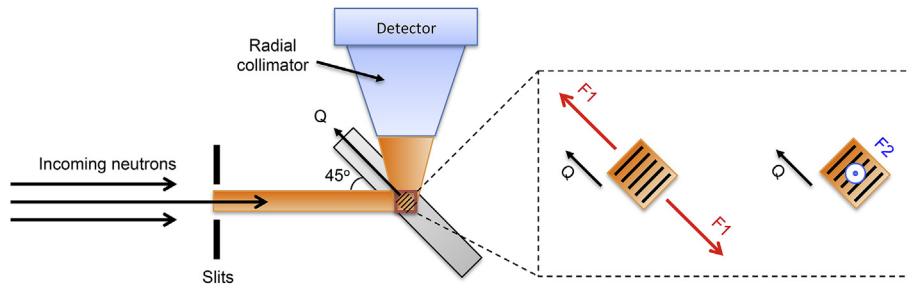


Fig. 5. Top view of the diffraction setup. The inset shows the relationship between loading direction and scattering vector Q .

$$\varepsilon_{hkl} = \frac{d_{hkl} - d_{hkl}^0}{d_{hkl}^0} \quad (4)$$

The peak broadening is expressed by the relative peak width:

$$w_{hkl} = \frac{\Delta d_{hkl}}{d_{hkl}} = \frac{\Delta Q_{hkl}}{Q_{hkl}} \quad (5)$$

with Δd_{hkl} and ΔQ_{hkl} the full-width at half-maximum of the hkl -diffraction peak. Both the resolution function of the instrument and the diffraction peaks after plastic deformation are well described by Gaussian functions. Therefore it is straightforward to separate the contribution from instrument (w_{hkl}^{instr}) and sample (w_{hkl}^{sample}) to the total peak broadening (w_{hkl}^{meas}):

$$w_{hkl}^{sample} = \sqrt{(w_{hkl}^{meas})^2 - (w_{hkl}^{instr})^2} \quad (6)$$

Fig. 6 (in web version) displays a typical diffraction pattern with fit. The inset shows a zoom in for the {200} peak demonstrating the quality of the fit.

2.5. Loading schemes

Various in situ experiments with different load schemes have been performed. The corresponding load paths are schematically shown in Fig. 7. In tests A and B the sample is loaded monotonically and then unloaded. In test A the sample is loaded and unloaded

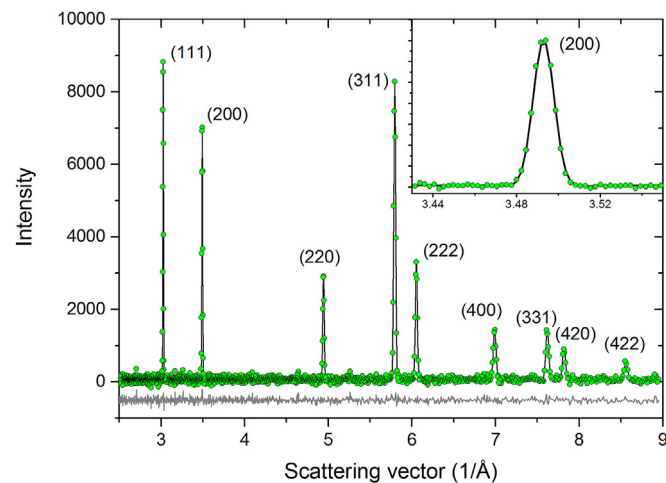


Fig. 6. Representative neutron diffraction pattern: experimental data (green circles), the fit profile (solid black line) and the residuals (solid grey line). The inset represents a zoom of the {200} diffraction peak. (For interpretation of the references to colour in this figure legend, the reader is referred to the web version of this article.)

along axis 1, while the load at the second axis is kept constant at 300 N (~3 MPa). Test B is an equibiaxial test where both axes are driven with the same force rate. All other tests involve strain path changes. The tests shown in Fig. 7 C and D both involve a uniaxial straining along one axis, followed by an uniaxial straining along the other axis and equibiaxial unloading. In test E the sample is unloaded after the first uniaxial loading cycle prior to loading and unloading along the second axis. In the last experiment (Fig. 7f) the sample is loaded uniaxially along axis 1, followed by a simultaneous unloading and loading along axis 1 and 2, respectively. Finally axis 1 is reloaded to arrive at an equibiaxial stress state. Unfortunately, no unload information is available for this last experiment.

3. Results

3.1. Effect of sample geometry

Evaluating the stress state at the centre of a cruciform shaped specimen with non-uniform thickness is not as straightforward as compared to a dogbone shaped specimen. First, the sample has no well-defined cross-section. Second, it is documented in literature that the circular thickness reduction at the centre of the sample causes a so-called 'ring effect' [39,40]. This can be easily understood considering a uniaxial deformation test on a cruciform shaped specimen (see also test A in Fig. 7). By pulling along axis 1 the stiffer ring that surrounds the centre region of the specimen deforms to an elliptical shape, which induces a compressive stress along axis 2. With other words, the central region is subjected to a 'geometrical' Poisson effect. As a consequence, the ratio between the applied forces along both axes cannot be 1 to 1 translated to the ratio of the applied stresses at the centre of the cruciform sample except for an equibiaxial test where both axes are affected equally. This effect is also well captured by our FEM simulations.

The ring effect has influence on several macroscopic parameters. During uniaxial deformation of the cruciform samples the apparent elastic Poisson's ratio is $\nu_{app} = 0.49 \pm 0.01$, whereas a value of $\nu = 0.30 \pm 0.03$ was found for the dogbone shaped specimen. Assuming a plane stress state for the cruciform specimen it can easily be shown that the ratio between the stress components is given by:

$$\frac{\sigma_{22}}{\sigma_{11}} = \frac{\nu_{app} - \nu}{1 - \nu \cdot \nu_{app}} = -0.23 \quad (7)$$

Our ABAQUS FEM simulations (see Fig. 2b) confirm this ratio. With other words, during 'uniaxial' deformation of the cruciform samples a biaxial stress state is generated at the centre of the sample.

A second effect occurs during the elastic–plastic transition. Here the ratio between stress components rapidly changes. This is apparent when plotting the evolution of the lattice strain as a function of applied force. Fig. 8 shows the evolution of the {311}

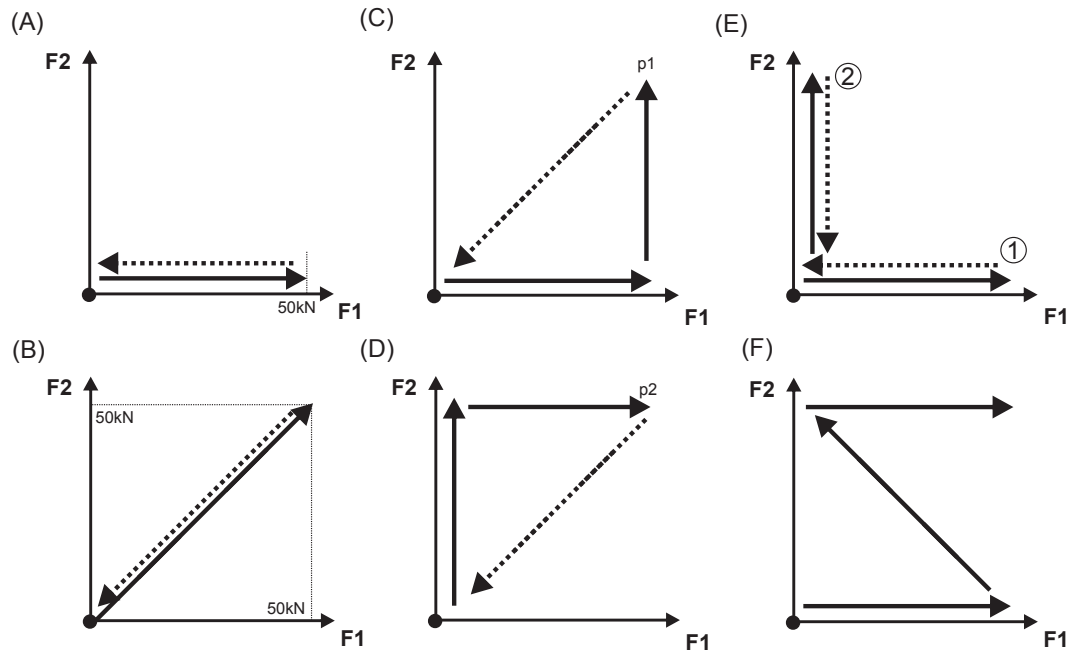


Fig. 7. Schematic overview of the various loading paths during the in situ neutron diffraction experiments.

grain family as a function of applied force along axis 1 during a uniaxial deformation test on a cruciform shaped specimen. We have chosen the {311} grain family as it is known to be most representative for the macroscopic stress state [41,42]. At a force of about 21 kN a clear deviation from linear elastic behaviour can be observed.

To exclude the possibility that such behaviour is not arising from the development of microstresses, multiple FE simulations were performed assuming isotropic, pure kinematic and combined non-linear isotropic and kinematic hardening. Experimental stress and strain data obtained from uniaxial dogbone tests were used as input for the hardening models. Henceforth, only the simulation results using the non-linear kinematic hardening model (Chaboche) with five backstresses are shown; from all the hardening models tested, this gives the best fit for the experimental elastic–plastic transition and the plastic regimes. The blue dashed line in Fig. 8 represents the simulated macroscopic elastic strain ϵ_{11}^e and describes very well the

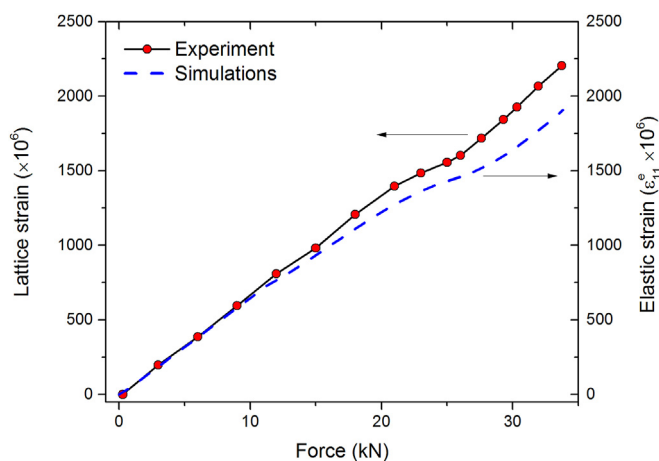


Fig. 8. Experimental lattice strain of the {311} grain family and the simulated macroscopic elastic strain as a function of applied force.

observed deviation from linearity, confirming that this is a purely geometrical effect. Interestingly, using different hardening models only result in a change in magnitude of Cauchy stresses, but the kink in lattice strain evolution is found to be independent of the hardening model. The simulations reveal that at the initiation of the elastic–plastic transition region, the elastic strain component in the axial direction (ϵ_{11}^e) increases slower than in the elastic regime. Meanwhile, the elastic strain component in the transverse direction (ϵ_{22}^e) has a negligible change in its evolution rate. Due to the Poisson effect, this results in a slower evolution of the σ_{11} , and faster evolution of σ_{22} .

Given the complex sample geometry the question arises how to convert the applied forces to the local stress state at the centre of the cruciform sample. This can be achieved by defining a so-called effective cross-section, which is however a non-trivial task. Our FEM simulations indicate that the effective cross-section actually changes significantly during the deformation test (in particular in the elastic–plastic transition regime). It is therefore crucial that appropriate hardening models are used, in particular for tests including a strain path change. An in-depth study of the relationship between applied forces and local stress state during deformation is however beyond the scope of this work.

For the monotonic tests (tests A and B in Fig. 7) we use the results from the FEM modelling to convert the applied force to the local stress state. Fig. 9 displays the von Mises equivalent stress as a function of accumulated plastic strain for the uniaxial tests on a dogbone and cruciform sample (test A) and for the equibiaxial test (test B). The agreement between the curves is reasonably good at low strain values. For larger strain values small deviations are observed.

As shown in section 2.2 the samples exhibit a mild rolling texture. This may complicate data analysis when changing strain path. In order to investigate the importance of the texture two uniaxial experiments on cruciform samples have been performed, the only difference being a sample rotation of 90°. Fig. 10 (left) compares the mechanical response for both experiments. Within the error of the measurement both stress–strain curve are the

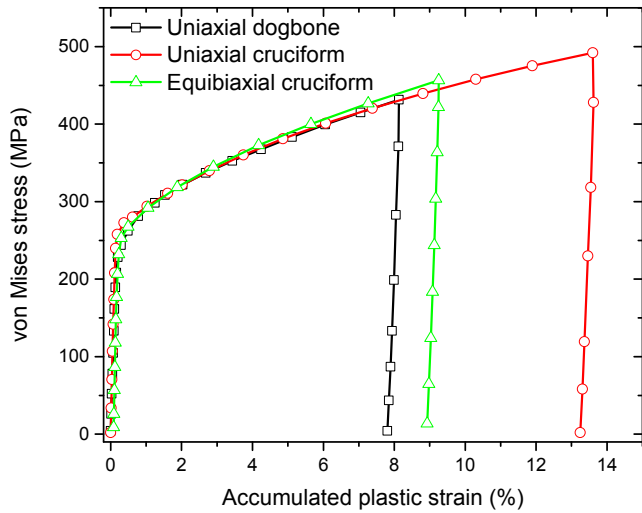


Fig. 9. Comparison of the mechanical response during a uniaxial deformation test on dogbone and cruciform shaped specimens.

same. On the right the lattice strain averaged over the $\{111\}$, $\{200\}$, $\{220\}$ and $\{311\}$ grain families is shown as a function of applied stress. Again, little difference is observed. Therefore the influence of initial texture is not further considered for this work. It should be noted that all other experiments reported in this work have been performed with the rolling direction aligned with axis 1.

3.2. Uniaxial versus equibiaxial

Fig. 11 compares the evolution of the lattice strain for the $\{111\}$ and $\{200\}$ diffraction peaks for uniaxial and equibiaxial deformation. The curve for the $\{220\}$ diffraction peak is omitted as its intensity drops significant during plastic deformation (see also further). The behaviour of the $\{311\}$ is very similar to that of $\{111\}$. The slopes in the elastic regime are obviously different. This can easily be understood considering that for the uniaxial case the relation between lattice strain along the horizontal axis and local stress is given by:

$$\varepsilon_{hkl} = \frac{\sigma_{11}}{E_{hkl}} \quad (8)$$

with E_{hkl} the hkl elastic modulus, whereas for the equibiaxial case the Poisson's ratio ν_{hkl} has to be taken into account:

$$\varepsilon_{hkl} = \frac{1 - \nu_{hkl}}{E_{hkl}} \sigma_{11} \quad (9)$$

Upon yielding the slopes deviate from their initial linear behaviour, indicative for a load transfer occurring between the different grain families. For the $\{200\}$ grain family we can notice that this deviation occurs in opposite directions; in the uniaxial case lattice strain accumulates faster compared to the elastic regime whereas the opposite is true for the equibiaxial case. The $\{111\}$ grain family exhibits only small deviations from linearity; here such a trend is more difficult to discern. This becomes clearer when comparing the residual lattice strains. Table 1 lists for the three grain families the residual lattice strain measured along axis 1 after unloading. The residual intergranular strains are the largest in the dogbone sample. After uniaxial straining of the cruciform shaped sample the residual strains are reduced, despite larger plastic strains are achieved (Fig. 9). For the equibiaxial case the residual lattice strains exhibit opposite signs as compared to the other two tests.

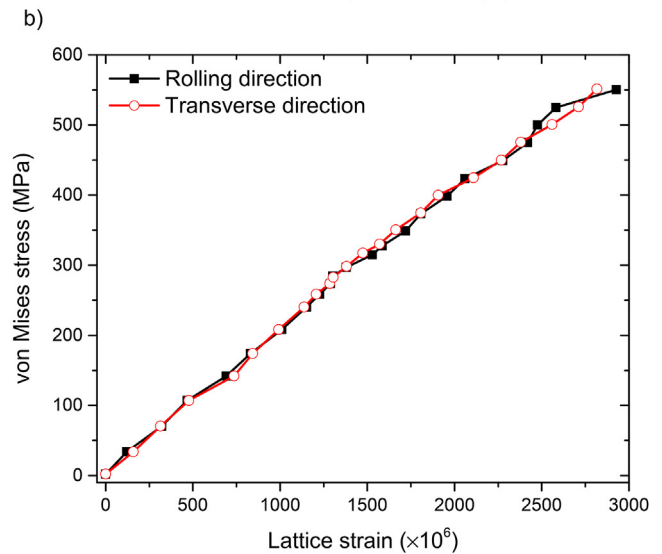
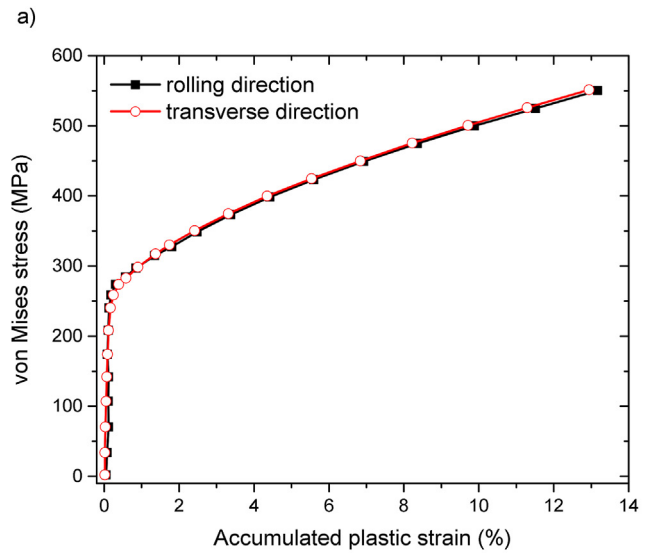


Fig. 10. Comparison of the mechanical response (a) and averaged axial lattice strain (b) for a uniaxial deformation tests on two cruciform samples rotated 90° compared to each other.

Fig. 12 displays the evolution of peak broadening as a function of accumulated plastic strain for the three continuous tests described above. During the initial stages of plastic deformation a strong increase in peak broadening is observed followed by a nearly linear regime. Interestingly the curves completely overlap, with other words, the peak broadening during monotonic loading is independent of the loading conditions and depends solely on the plastic strain.

Fig. 13 compares the evolution of the integrated intensity during uniaxial loading (full lines) and equibiaxial loading (dashed lines). During equibiaxial loading little change is observed, which suggests relatively little change in texture. For the uniaxial case the $\{111\}$ and $\{200\}$ grain families exhibit a strong increase of integrated intensity, at the expense of the $\{311\}$ and $\{220\}$ grain families.

3.3. Strain path changes

We now compare the results obtained in the tests shown in Figs. 6c, 6d, 6e and 6f. As the local macroscopic stress states after changing the strain paths are unknown, the evolution of the peak

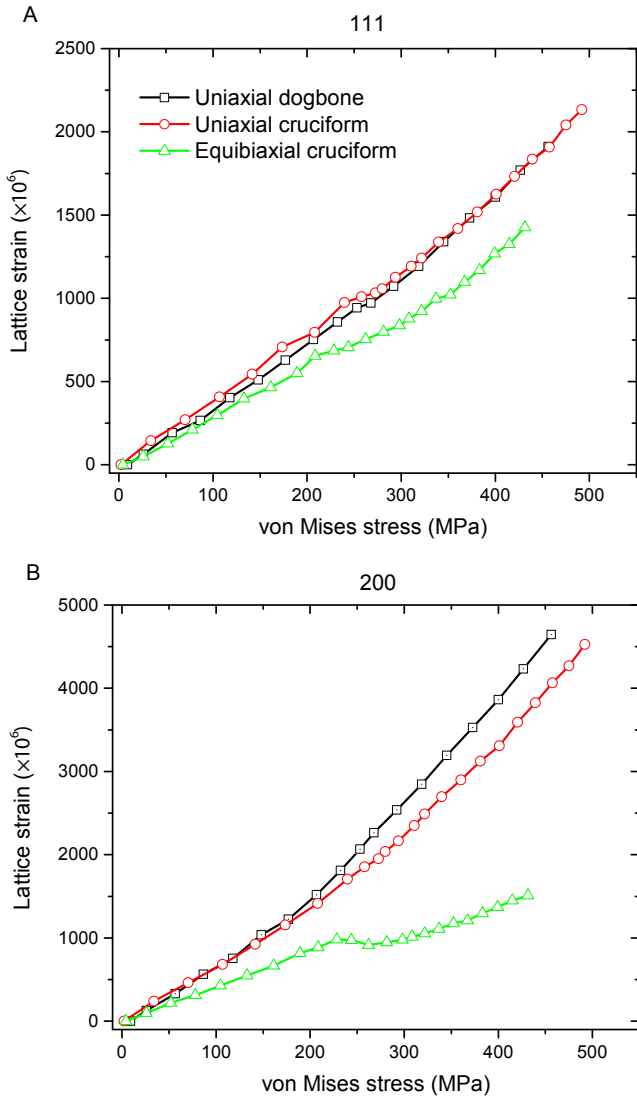


Fig. 11. Lattice strain of the {111} and {200} grain family as a function of applied stress. The unloads are not shown for clarity.

Table 1

Grain family	Lattice strain ($\times 10^6$)		
	1:0 dogbone	1:0 cruciform	1:1 cruciform
{111}	-63	-180	48
{200}	1265	600	-330
{311}	460	315	-100

broadening is plotted as a function of lattice strain. In what follows we restrict the plots to the {200} grain family which exhibits the strongest effects. The observed behaviour of the other grain families is qualitatively similar.

Fig. 14 (in web version) compares the evolution of the {200} peak broadening for tests C and D (Fig. 6). These two tests are the same from a mechanical point of view. However, in one case (test C) the scattering vector is parallel to the initial loading direction, where for test D it is perpendicular. With other words, for the pre-straining part the neutron signal captures the nominal axial and transverse response for tests C and D, respectively. As expected in the elastic regime no peak broadening is observed. Note that the

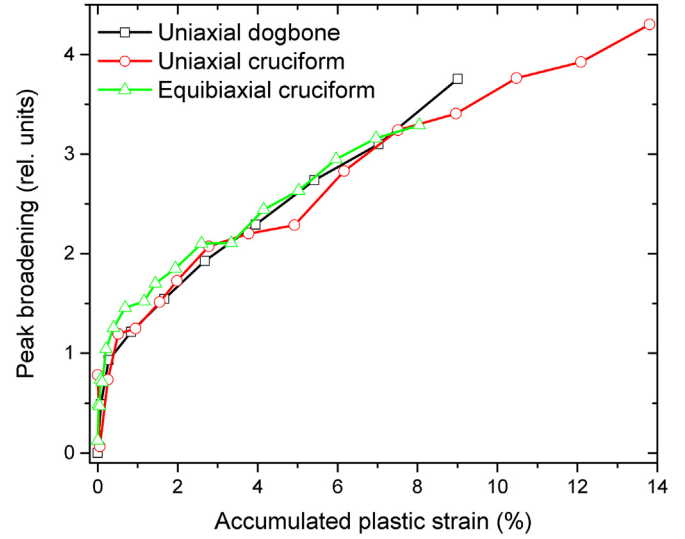


Fig. 12. Peak broadening of the {200} grain family as a function of von Mises strain for the continuous uniaxial tests on dogbone and cruciform specimen and for the equibiaxial test.

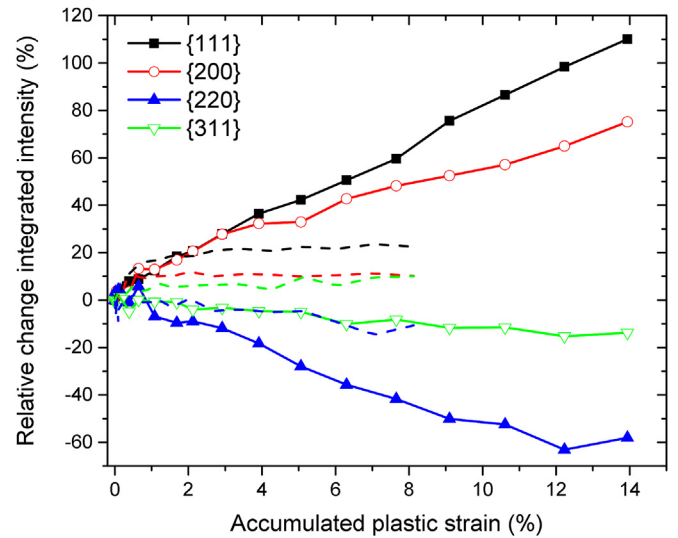


Fig. 13. Change of integrated intensity for various grain families during uniaxial (full lines) and equibiaxial (dashed lines) loading.

relatively large scatter in this regime is related to the deconvolution procedure (equation (6)). The peak width prior to convolution exhibits a smooth behaviour. Upon yielding the peak width increases significantly, indicative for an increasing dislocation density. When activating the second axis not only the magnitude of the lattice strains reduces but also the peak broadening clearly decreases. Irrespectively of the followed load path at the final stress state both lattice strain and peak broadening are very similar. Note that for clarity the evolution during unloading is not shown. Here the peak broadening essentially remains flat. The final values for peak broadening and lattice strain after unloading are given by the red and blue triangle.

Fig. 15 displays the evolution of the {200} peak broadening as a function of lattice strains for tests E and F. Similar observations as for the tests C and D can be made: upon changing the strain path the peak broadening clearly decreases. Interestingly, the decrease is initially very similar for tests E and F, although the local stress state

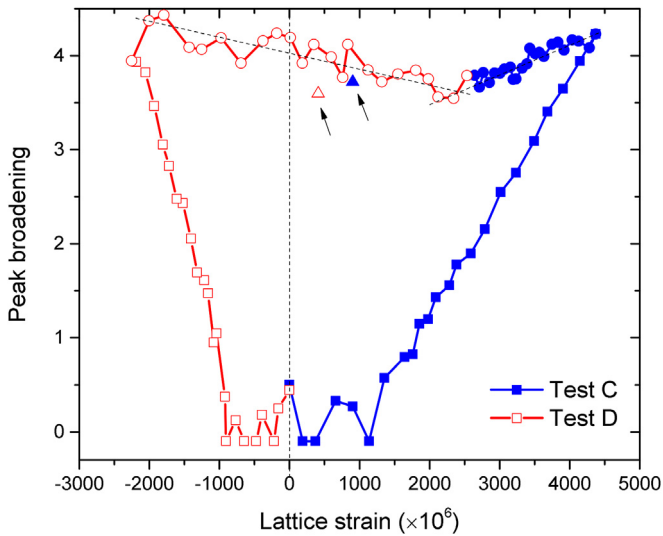


Fig. 14. Peak broadening of the {200} grain family as a function of lattice strain for tests C and D. The data points during the final unloading are not shown for clarity. The red and blue triangles (also indicated by the black arrows) represent the positions at the end of the test. The dashed lines represent guides for the eye. (For interpretation of the references to colour in this figure legend, the reader is referred to the web version of this article.)

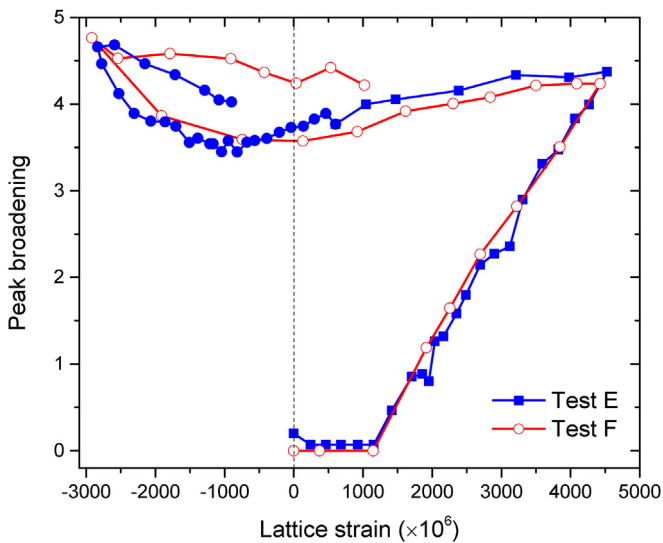


Fig. 15. Comparison of the evolution of the {200} peak broadening for the tests E and F. For test E the first and second load/unload sequences are indicated by squares and circles, respectively.

is quite different. A second important observation is that for test E the peak broadening continues to decrease upon reloading along the second direction until a lattice strain of -1000 .

Fig. 16a shows the evolution of the integrated intensities as a function of accumulated plastic strain for test E (90° strain path change). The onset of the second load is indicated by the black dashed line. Upon changing the strain path the slopes of the curves exhibit the same magnitude but with opposite sign. With other words, the texture evolution is reversed. Unfortunately no such plot can be made for test F as the 3D-DIC data is missing. In order to compare the intensity evolution for test E and F we plot the integrated intensity as a function of peak broadening for the {111} peak (Fig. 16b). Both curves exhibit very similar trends: with increasing peak broadening the intensity of the 111 peak increases. When the

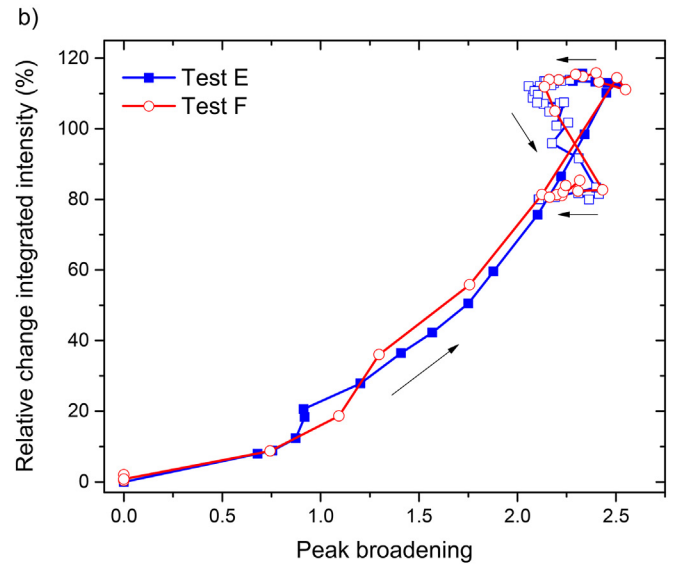
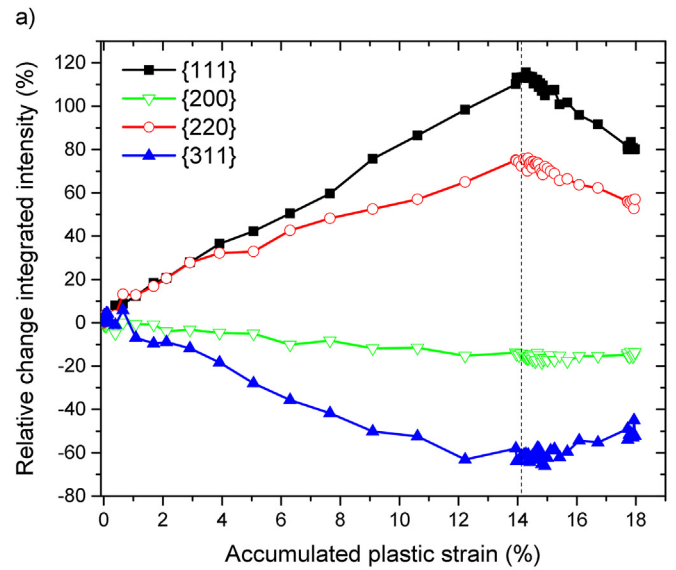


Fig. 16. (a) Relative change of integrated intensities as a function of accumulated plastic strain for test E. The black dashed line indicates the onset of the second load. (b) Relative change of integrated intensity of the {111} peak versus peak broadening for tests E and test F. For test E the closed and open symbols represent the first and second part of the loading sequence. (For interpretation of the references to colour in this figure legend, the reader is referred to the web version of this article.)

peak broadening decreases (see also Fig. 15) the intensity remains constant. Only when the peak broadening increases again the intensity starts decreasing. During the final stages of test E and F again the decrease in peak broadening is not accompanied by any change in intensity.

4. Discussion

4.1. Assessment of the new deformation rig

In this work we have presented a new multiaxial deformation rig, which exhibits two perpendicular loading axes that can be operated independent from each other. This allows performing in-plane biaxial straining of cruciform shaped specimen with various load ratios and/or complex strain path changes. The sample geometry chosen for this work (Fig. 2) has the advantage that 1) large

plastic deformation is possible before failure at the notches and 2) plasticity occurs in the region probed by the neutrons. It however also bears additional complexity: because of the ring effect the ratio of the applied loads along the two axes is not equal to the ratio of the local stress components (section 3.1). This has to be taken into account when specific load ratios are desired. Also the conversion of applied force into applied stress is non trivial and requires the aid of FEM modelling. While this seems to work reasonably well for monotonic loading (section 3.1) it becomes more complex for the case of strain path changes. Here a detailed knowledge on how the yield surface is moving and changing its shape is required. This can be achieved with the help of distortional plasticity models which allow the yield surface to expand/contract, translate, distort and rotate (see, for instance, Refs. [43,44,6]). This however is beyond the scope of the present work.

4.2. Monotonic loading

During uniaxial and equibiaxial straining, the lattice strains respond linearly to the applied stress in the elastic regime. The different slopes for the different grain families reflect the elastic anisotropy of 316 L steel. Upon yielding the slopes deviate from this initial linear behaviour. Here a load transfer occurs between the different grain families; due to plastic anisotropy some grain families are plastically ‘softer’ compared to others [8–10]. As a consequence the local stress accumulation in these grains is lower as compared to the average bulk behaviour. The opposite is the case for the harder grain families. Which families are soft(er) and which are hard(er) depends on the material’s elastic constants, texture and plastic anisotropy (e.g. average Schmid factor, number of activated slip systems, etc.). Such a load transfer causes residual intergranular strain upon unloading.

In this work we have shown how the ε_1 lattice strain component along axis 1 strongly depends on the nature of applied stress. The effect is most pronounced for the {200} grain family; during uniaxial deformation tensile strains develop, whereas during biaxial deformation compressive strains arise. Qualitatively this result can be understood as follows. Let’s consider the normalized strain tensors for uniaxial (equation (10)) and equibiaxial (equation (11)) straining:

$$\varepsilon^N = \begin{pmatrix} \sqrt{\frac{2}{3}} & 0 & 0 \\ 0 & -\sqrt{\frac{2}{12}} & 0 \\ 0 & 0 & -\sqrt{\frac{2}{12}} \end{pmatrix} \quad (10)$$

$$\varepsilon^N = \begin{pmatrix} \frac{1}{\sqrt{6}} & 0 & 0 \\ 0 & \frac{1}{\sqrt{6}} & 0 \\ 0 & 0 & -\frac{2}{\sqrt{6}} \end{pmatrix} \quad (11)$$

From equation (11) it becomes immediately apparent that equibiaxial straining along axes 1 and 2 has the same normalized strain tensor as a uniaxial compression experiment in a direction perpendicular to the plane of the sample. With other words the observed lattice strain qualitatively corresponds to the transverse response of a uniaxial compression test. Therefore it is expected that after biaxial straining the sign of the residual strain component along axis 1 is reversed compared to uniaxial straining (see, for

instance, Ref. [14]). However, in order to fully grasp the origin and magnitude of the observed residual strains crystal plasticity modeling is needed.

Fig. 12 demonstrates that the peak broadening depends mainly on the amount of plastic strain and is not sensitive to the applied stress state. It can be expected that the main cause for peak broadening be related to a dislocation mechanism. However, 316 L stainless steel is known to have an intermediate value for the stacking fault energy (~ 60 mJ/m²). Therefore twinning cannot be excluded as a secondary deformation mechanism [45,46]. To establish whether our peak broadening is mainly related to dislocations we have studied the Williamson–Hall (WH) plot at the end of test A (i.e. after 13% plastic strain). This is shown in Fig. 17 (in web version) by the black squares. The red circles represent the modified WH plot where the dislocation contrast factor C is taken into account [47]. The fact that all points follow a parabolic curve (represented by the red line) is a strong indication that dislocations are the main cause for peak broadening in these samples [48–50]. Note that this does not exclude that twinning does not occur, it merely means that twinning is not the dominant factor in peak broadening.

The evolution of the integrated intensities during uniaxial straining (Fig. 13) is in good agreement with a $\langle 111 \rangle$ and $\langle 100 \rangle$ double fiber texture parallel to the loading axis, characteristic for fcc materials. For biaxial stretching no particular in-plane texture evolution is expected. A similar argument as above applies; the strain for equibiaxial stretching is identical to that of uniaxial compression and therefore also the texture evolution is expected to be similar, which is for fcc materials typically a fiber texture with $\langle 011 \rangle$ normal to the compressive plane [51]. The scattering vector for this experiment lies in the plane of the sample. Therefore little change in integrated intensities are expected.

4.3. Recovery during strain path changes

A change in strain path has a noticeable impact on the mechanical behaviour and microstructural development, especially

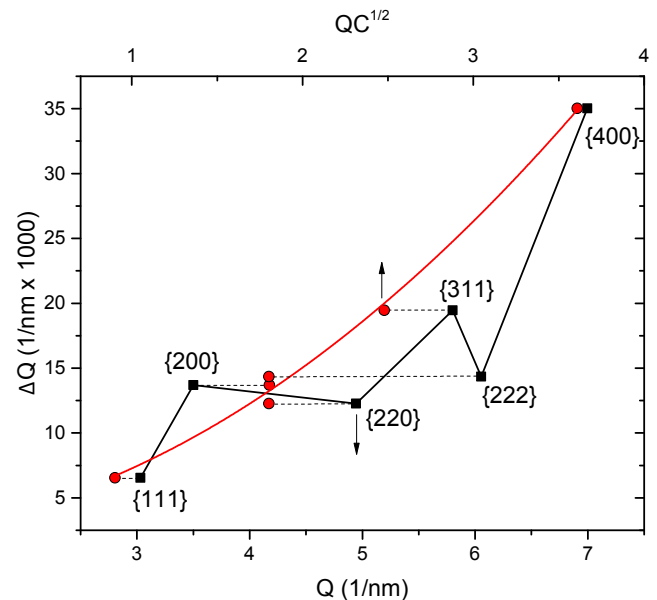


Fig. 17. Regular (black squares) and modified (red circles) Williamson-Hall plot recorded at the end of test A. The red line represents a parabolic fit through the red data points. (For interpretation of the references to colour in this figure legend, the reader is referred to the web version of this article.)

the dislocation substructure. During pre-straining the yield surface grows and shifts due to isotropic and kinematic hardening [52]. However, for the strain path changes performed in this work (tests C–F) the exact evolution of yield surface is not known. Assuming that 1) the yield surface does not change shape i.e. only kinematic or isotropic hardening occurs and 2) the associative flow rule applies i.e. the plastic strain rate at any point on the yield surface is normal to the tangent at that point, the evolution of the yield surface can be intuitively drawn as shown in Fig. 18 (in web version).

The blue ellipse represents the 2D yield surface prior to deformation. During uniaxial pre-straining (blue arrows in Fig. 18) the sample experiences a biaxial stress due the ring effect. Therefore the blue arrow makes an angle with respect to σ_1 axis. Due to isotropic and kinematic hardening the yield surface grows and shifts in the direction of the pre-straining. The red ellipse represents the yield surface at the end of pre-straining. For the tests C and D the second load path remains mostly elastic. This is visualized by the red arrow in Fig. 18A, which lies within the yield surface. Therefore, only ~0.3% plastic strain is being generated. During test E the sample is first unloaded and then reloaded in a direction perpendicular to the first direction. Again here the ring effect is expected to play an important role. Because of the kinematic hardening yielding occurs at a lower von Mises stress as compared to the end of the pre-straining.

The magnitude of the strain path change is usually expressed by the parameter $\cos \zeta$, which is defined as:

$$\cos \zeta = \frac{\dot{\epsilon}_1^p : \dot{\epsilon}_2^p}{\|\dot{\epsilon}_1^p\| \|\dot{\epsilon}_2^p\|} \quad (12)$$

with $\dot{\epsilon}_n^p$ the plastic strain rate along axis n . For a 90° strain path change $\cos \zeta$ would be about -0.5 . However, due the ring effect the angles between the plastic strain rates at the end of pre-straining and at yield during reloading will be higher. This is schematically shown in Fig. 18B by the black arrows. This leads to lower values for $\cos \zeta$, more towards the value for a regular tension-compression Bauschinger test ($\cos \zeta = -1$). It can therefore be anticipated that during reloading many slip systems that were operating during pre-straining are again operative, however now with dislocations moving in opposite directions [3]. This hypothesis is strengthened by the evolution of the integrated intensities which are a measure for the texture evolution (see Fig. 16a); upon reloading the texture evolves in opposite direction at the same rate as a function of

plastic compared to pre-straining. For test F a similar picture can be drawn: because of kinematic hardening early yielding occurs during reloading (blue-red arrow in Fig. 18C). It can be anticipated that yielding will occur at similar von Mises stress as compared to test E.

As mentioned, mechanical twinning may exist besides dislocation slip. In that case part of the observed hardening during pre-straining is partly due to dislocation–twin interactions. After a strain path change the new active dislocation slip systems have a different orientation to the twin planes, which may increase the mean slip length of the new active dislocations. This leads to a reduction of the pile-up stresses at the beginning of reloading, which in turn results in a lower yield stress. This has been demonstrated experimentally by Sakharova et al. [53].

Diffraction peak broadening may have various origins [50]. For this study the relevant contributions are: i) dislocations and/or elastic strain gradients (type III strains) and ii) distribution of intergranular strains within a grain family (type II strains). Grain size effects are not expected to contribute significantly to the diffraction peak broadening. Therefore, during a strain path the evolution of the peak broadening will be the net result of a competition between various effects: i) a decreasing peak width due to an reduction of type III stresses related to the backflow of dislocations or generation of dislocations with opposite sign which annihilate with existing dislocations, ii) a change in the width of the distribution of intergranular strains and iii) an increase in dislocation density on newly activated slip systems with accompanying latent hardening [8–10].

This competition is visualized by comparing tests C–F. In the tests C and D no increase in dislocation density is expected during the second loading sequence. Here only a decreasing peak broadening is observed. In contrast, for tests E and F the reloading is composed of an elastic and plastic part. Here the peak broadening first decreases, during which no change in integrated intensity is observed, following an increasing peak width accompanied by a decreasing integrated intensity.

In order to shed more light on the possible mechanism responsible for the recovery in peak broadening we have performed an additional test. It consists of two consecutive uniaxial load/unload sequences, both to 60 kN. Fig. 19a shows the mechanical response. During the first sequence an equivalent strain of 21% is reached whereas after the second load about 0.5% plastic strain is generated. The evolution of the peak broadening as a function of lattice strain is shown in Fig. 19b. Similar to the results for test E the peak broadening decreases during unloading. During reloading the peak broadening initially remains constant before

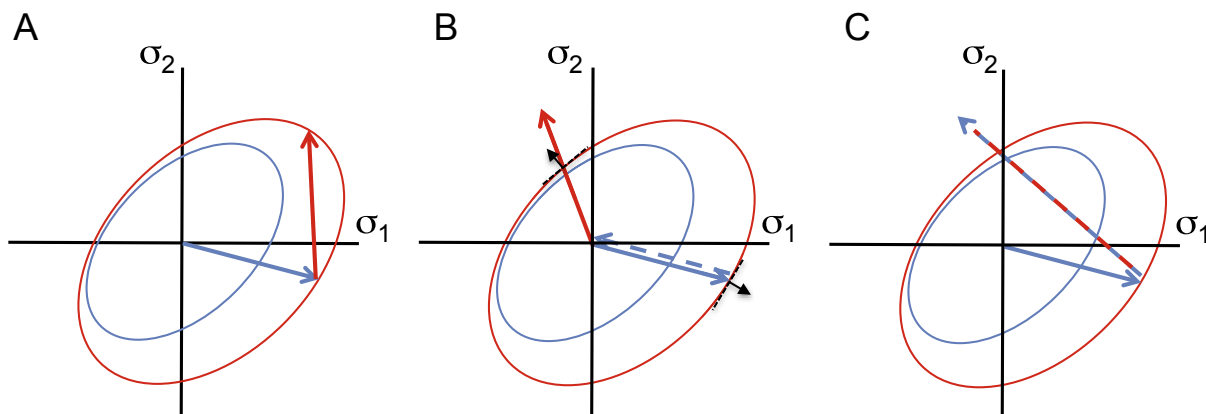


Fig. 18. Schematic view of 2D yield surfaces. The blue and red ellipsoids represent yield surfaces prior and at the end of pre-straining. The black arrows in B indicate the direction of the plastic strain rates. (For interpretation of the references to colour in this figure legend, the reader is referred to the web version of this article.)

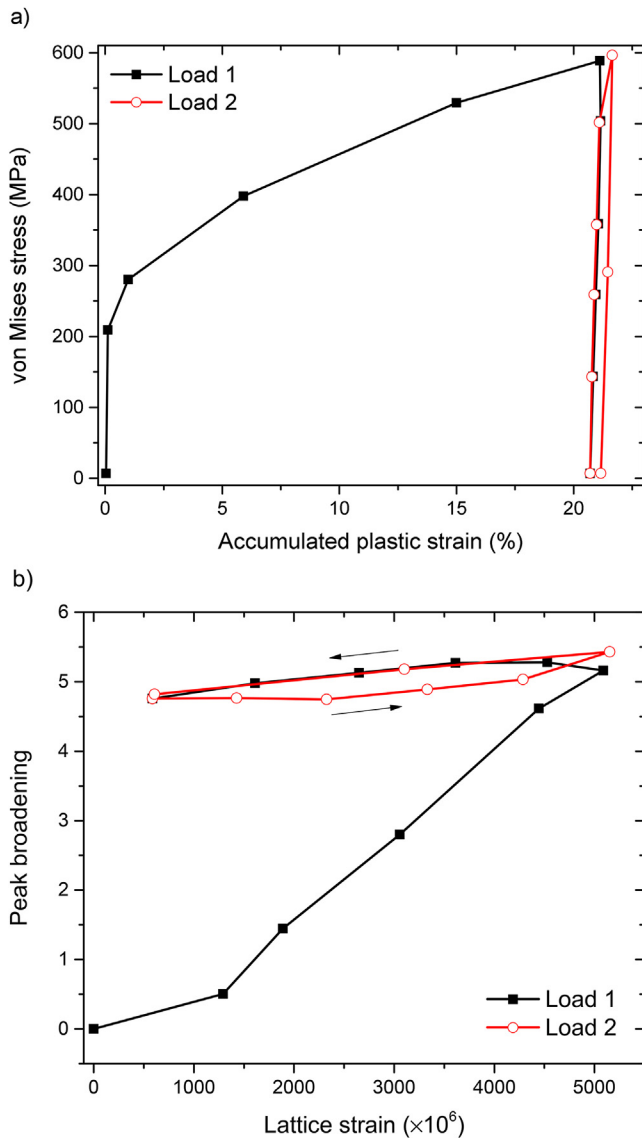


Fig. 19. Mechanical data for two consecutive uniaxial load/unload sequences (left) with the corresponding evolution of peak broadening as a function of lattice strain for the {200} grain family.

increasing towards the same level compared to the end of the first loading cycle. The “hysteresis” in the peak broadening is an indication that the initial recovery during unloading induces permanent changes to the microstructure. Near the end of the reload the material yields again, which results in both the generation of plastic strain and an increase in peak broadening. Upon unloading the peak broadening follows basically the same path as compared to the first unloading. This confirms the following microstructural picture of Bauschinger effect in 316 L: during unloading dislocations that were piled-up at grain boundaries run back into the grain, thereby reducing local strain gradients. In the grain interior they may get pinned or annihilate. This process continues when reloading in a direction perpendicular to the original one. At the same time the stress distribution between members of the same grain family reduces, which may also contribute in part of the observed decrease in peak broadening. During reloading along the same direction dislocations get unpinned or new dislocations are generated causing micro yielding at stresses below the stress reached at the end of the previous load.

5. Summary and outlook

We have successfully implemented and tested a new biaxial deformation rig, which allows applying in-plane stress states and performing complex strain path changes under neutron diffraction. We have demonstrated that

- the sample shape has a profound influence on the resulting stress state and needs to be taken into account when evaluating the neutron diffraction data. We have shown the need for further optimizing the sample geometry in order to minimize the ring effect and the use of finite element modelling to convert applied forces into the local stress state in the gauge volume,
- the evolution of lattice strains for various grain families along a particular direction differs when deforming continuous uniaxial or equal biaxially. The observed difference can be explained intuitively. However, advanced crystal plasticity simulations will be needed in order to quantitatively capture the observed trends.
- The evolution of peak broadening during strain path changes sheds light on microstructural evolutions. We find significant recovery of the internal strains for a strain path change during both unloading and elastic reloading along a direction perpendicular to the original direction. This interesting observation challenges current state-of-art crystal plasticity models.
- It is now standard practice to calculate elastic lattice strains from crystal plasticity simulations. Recent attempts to perform similar calculations for diffraction peak broadening had only limited success [12,54]. This is mainly due to the fact that the stress contribution of individual dislocations cannot be taken into account, as is the case for discrete dislocation dynamics simulations. Based on the findings of this work we therefore advocate to strengthen the efforts to improve the calculation of realistic values for diffraction peak broadening from crystal plasticity simulations.

Acknowledgements

The development of the multiaxial deformation rig was supported by the Competence Centre for Materials Science and Technology (CCMX). HVS thanks the European Research Council for financial support within the ERC-advanced grant MULTIAX (339245). We thank the BSQ team at PSI for their high quality technical support and Dr. W. Wagner for his extended support in design and implementation. Finally we thank Prof. F. Barlat and Dr. M. Niffenegger for fruitful discussions.

References

- [1] I.J. Beyerlein, C.N. Tomé, Modeling transients in the mechanical response of copper due to strain path changes, *Int. J. Plasticity* 23 (2007) 640–664, <http://dx.doi.org/10.1016/j.jplas.2006.08.001>.
- [2] A. Abel, Historical perspectives and some of the main features of the Bauschinger effect, *Mater. Forum (Switzerland)* 10 (1987) 11–26.
- [3] J.H. Schmitt, J.V. Fernandes, J.J. Gracio, M.F. Vieira, M.F. Vieira, Plastic behaviour of copper sheets during sequential tension tests, *Mater. Sci. Eng. A* 147 (1991) 143–154, [http://dx.doi.org/10.1016/0921-5093\(91\)90840-J](http://dx.doi.org/10.1016/0921-5093(91)90840-J).
- [4] C. Wejdemann, H.F. Poulsen, U. Lienert, W. Pantleon, In situ observation of the dislocation structure evolution during a strain path change in copper, *JOM* 65 (2013) 35–43, <http://dx.doi.org/10.1007/s11837-012-0504-0>.
- [5] M.A. Iadicola, L. Hu, A.D. Rollett, T. Foecke, Crystal plasticity analysis of constitutive behavior of 5754 aluminum sheet deformed along bi-linear strain paths, *Int. J. Solids Struct.* 49 (2012) 3507–3516, <http://dx.doi.org/10.1016/j.jsolstr.2012.03.015>.
- [6] F. Barlat, J.J. Gracio, M.-G. Lee, E.F. Rauch, G. Vincze, An alternative to kinematic hardening in classical plasticity, *Int. J. Plasticity* 27 (2011) 1309–1327, <http://dx.doi.org/10.1016/j.jplas.2011.03.003>.
- [7] M.E. Kassner, P. Geantil, L.E. Levine, B.C. Larson, Backstress, the Bauschinger Effect and Cyclic Deformation, in: M. Cabibbo, S. Spigarelli (Eds.), *Recent Developments in the Processing and Applications of Structural Metals and Alloys*,

- Trans Tech Publications Ltd, Stafa-Zurich, 2009, pp. 39–51.
- [8] B. Clausen, T. Lorentzen, T. Leffers, Self-consistent modelling of the plastic deformation of f.c.c. polycrystals and its implications for diffraction measurements of internal stresses, *Acta Mater.* 46 (1998) 3087–3098, [http://dx.doi.org/10.1016/S1359-6454\(98\)00014-7](http://dx.doi.org/10.1016/S1359-6454(98)00014-7).
- [9] E.C. Oliver, M.R. Daymond, P.J. Withers, Interphase and intergranular stress generation in carbon steels, *Acta Mater.* 52 (2004) 1937–1951, <http://dx.doi.org/10.1016/j.actamat.2003.12.035>.
- [10] M.R. Daymond, H.G. Priesmeyer, Elastoplastic deformation of ferritic steel and cementite studied by neutron diffraction and self-consistent modelling, *Acta Mater.* 50 (2002) 1613–1626, [http://dx.doi.org/10.1016/S1359-6454\(02\)00026-5](http://dx.doi.org/10.1016/S1359-6454(02)00026-5).
- [11] H. Wang, P.D. Wu, C.N. Tomé, Y. Huang, A finite strain elastic–viscoplastic self-consistent model for polycrystalline materials, *J. Mech. Phys. Solids* 58 (2010) 594–612, <http://dx.doi.org/10.1016/j.jmps.2010.01.004>.
- [12] A.K. Kanjarla, R.A. Lebensohn, L. Balogh, C.N. Tome, Study of internal lattice strain distributions in stainless steel using a full-field elasto-viscoplastic formulation based on fast Fourier transforms, *Acta Mater.* 60 (2012) 3094–3106, <http://dx.doi.org/10.1016/j.actamat.2012.02.014>.
- [13] P.B. Prangnell, T. Downes, P.J. Withers, T. Lorentzen, An examination of the mean stress contribution to the Bauschinger effect by neutron diffraction, *Mater. Sci. Eng. A* 197 (1995) 215–221, [http://dx.doi.org/10.1016/0921-5093\(94\)09744-5](http://dx.doi.org/10.1016/0921-5093(94)09744-5).
- [14] B. Chen, J.N. Hu, Y.Q. Wang, S.Y. Zhang, S. Van Petegem, A.C.F. Cocks, et al., Role of the misfit stress between grains in the Bauschinger effect for a polycrystalline material, *Acta Mater.* 85 (2015) 229–242, <http://dx.doi.org/10.1016/j.actamat.2014.11.021>.
- [15] J.A. Wollmershauser, B. Clausen, S.R. Agnew, A slip system-based kinematic hardening model application to in situ neutron diffraction of cyclic deformation of austenitic stainless steel, *Int. J. Fatigue* 36 (2012) 181–193, <http://dx.doi.org/10.1016/j.ijfatigue.2011.07.008>.
- [16] J. Repper, M. Niffenegger, S. van Petegem, W. Wagner, H. van Swygenhoven, Biaxial mechanical testing at the neutron time-of-flight diffractometer POLDI, *Mater. Sci. Forum* 768–769 (2013) 60–65, <http://dx.doi.org/10.4028/www.scientific.net/MSF.768-769.60>.
- [17] T. Foecke, M.A. Iadicola, A. Lin, S.W. Banovic, A method for direct measurement of multiaxial stress-strain curves in sheet metal, *Metall. Mater. Trans. A Phys. Metall. Mater. Sci.* 38A (2007) 306–313, <http://dx.doi.org/10.1007/s11661-006-9044-y>.
- [18] M.A. Iadicola, T. Foecke, S.W. Banovic, Experimental observations of evolving yield loci in biaxially strained AA5754-O, *Int. J. Plasticity* 24 (2008) 2084–2101, <http://dx.doi.org/10.1016/j.ijplas.2008.03.003>.
- [19] M.A. Iadicola, A.A. Creuziger, T. Foecke, Advanced biaxial cruciform testing at the NIST Center for Automotive lightweighting, in: M. Rossi, M. Sasso, N. Connessor, R. Singh, A. DeWald, D. Backman, et al. (Eds.), *Residual Stress, Thermomechanics & Infrared Imaging, Hybrid Techniques and Inverse Problems*, 8, Springer International Publishing, 2014, pp. 277–285 (accessed 11.09.15.), http://link.springer.com/chapter/10.1007/978-3-319-00876-9_34.
- [20] V. Imbeni, A. Mehta, S.W. Robertson, T.W. Duerig, A.R. Pelton, R.O. Ritchie, *On the Mechanical Behavior of Nitinol under Multiaxial Loading Conditions and in Situ Synchrotron X-ray, Smst Soc Inc, Menlo Park, 2004*.
- [21] A. Mehta, X.-Y. Gong, V. Imbeni, A.R. Pelton, R.O. Ritchie, Understanding the Deformation and fracture of nitinol endovascular stents using in situ synchrotron X-ray microdiffraction, *Adv. Mater.* 19 (2007) 1183–1186, <http://dx.doi.org/10.1002/adma.200601916>.
- [22] D. Gonzalez, J.F. Kelleher, J. Quinta da Fonseca, P.J. Withers, Macro and intergranular stress responses of austenitic stainless steel to 90° strain path changes, *Mater. Sci. Eng. A* 546 (2012) 263–271, <http://dx.doi.org/10.1016/j.msea.2012.03.064>.
- [23] D.M. Collins, M. Mostafavi, R.I. Todd, T. Connolly, A.J. Wilkinson, A synchrotron X-ray diffraction study of in situ biaxial deformation, *Acta Mater.* 90 (2015) 46–58, <http://dx.doi.org/10.1016/j.actamat.2015.02.009>.
- [24] C. Wejdemann, H.F. Poulsen, U. Lienert, W. Pantleon, The Effect of strain path change on subgrain volume fraction determined from in situ X-ray measurements, *Dislocations* 2008 3 (2009) 012003, <http://dx.doi.org/10.1088/1757-899X/3/1/012003>.
- [25] W. Pantleon, C. Wejdemann, B. Jakobsen, U. Lienert, H.F. Poulsen, Evolution of deformation structures under varying loading conditions followed in situ by high angular resolution 3DXRD, *Mater. Sci. Eng. A Struct. Mater. Prop. Microstruct. Process.* 524 (2009) 55–63, <http://dx.doi.org/10.1016/j.msea.2009.04.008>.
- [26] C. Wejdemann, U. Lienert, W. Pantleon, Reversal of asymmetry of X-ray peak profiles from individual grains during a strain path change, *Scr. Mater.* 62 (2010) 794–797, <http://dx.doi.org/10.1016/j.scriptamat.2010.01.032>.
- [27] G. Geandier, D. Thiaudiere, R.N. Randriamazaoro, R. Chiron, S. Djaziri, B. Lamongie, et al., Development of a synchrotron biaxial tensile device for in situ characterization of thin films mechanical response, *Rev. Sci. Instrum.* 81 (2010) 103903, <http://dx.doi.org/10.1063/1.3488628>.
- [28] G. Geandier, D. Faurie, P.-O. Renault, D. Thiaudiere, E. Le Bourhis, In situ monitoring of X-ray strain pole figures of a biaxially deformed ultra-thin film on a flexible substrate, *J. Appl. Crystallogr.* 47 (2014) 181–187, <http://dx.doi.org/10.1107/S1600576713030720>.
- [29] O. Benafan, S.A. Padula, H.D. Skorpenske, K. An, R. Vaidyanathan, Design and implementation of a multiaxial loading capability during heating on an engineering neutron diffractometer, *Rev. Sci. Instrum.* 85 (2014) 103901, <http://dx.doi.org/10.1063/1.4896042>.
- [30] E. Cakmak, H. Choo, J.-Y. Kang, Y. Ren, Relationships between the phase transformation kinetics, texture evolution, and microstructure development in a 304L stainless steel under biaxial loading conditions: synchrotron X-ray and electron backscatter diffraction Studies, *Metall. Mater. Trans. A* 46 (2015) 1860–1877, <http://dx.doi.org/10.1007/s11661-015-2772-0>.
- [31] L. Andrusca, V. Goanta, P.D. Barsanescu, Optimizing the shape and size of cruciform specimens used for biaxial tensile test, *Appl. Mech. Mater.* (Switzerland) 658 (2014) 167–172, <http://dx.doi.org/10.4028/www.scientific.net/AMM.658.167>.
- [32] A. Hannon, P. Tiernan, A review of planar biaxial tensile test systems for sheet metal, *J. Mater. Process. Technol.* 198 (2008) 1–13, <http://dx.doi.org/10.1016/j.jmatprotec.2007.10.015>.
- [33] D.E. Green, K.W. Neale, S.R. MacEwen, A. Makinde, R. Perrin, Experimental investigation of the biaxial behaviour of an aluminum sheet, *Int. J. Plasticity* 20 (2004) 1677–1706, <http://dx.doi.org/10.1016/j.ijplas.2003.11.012>.
- [34] Gerard Quaak, *Biaxial Testing of Sheet Metal: an Experimental-numerical Analysis, Master thesis, Eindhoven University of Technology, 2008*.
- [35] ABAQUS Documentation, Dassault Systèmes, Providence, RI (USA), 2011.
- [36] U. Stuhr, Time-of-flight diffraction with multiple pulse overlap. Part I: the concept, nuclear instruments and methods in physics research section a: accelerators, spectrometers, *Detect. Assoc. Equip.* 545 (2005) 319–329, <http://dx.doi.org/10.1016/j.nima.2005.01.320>.
- [37] U. Stuhr, H. Spitzer, J. Egger, A. Hofer, P. Rasmussen, D. Graf, et al., Time-of-flight diffraction with multiple frame overlap Part II: The strain scanner POLDI at PSI, nuclear instruments and methods in physics research section a: accelerators, spectrometers, *Detect. Assoc. Equip.* 545 (2005) 330–338, <http://dx.doi.org/10.1016/j.nima.2005.01.321>.
- [38] O. Arnold, J.C. Bilheux, J.M. Borreguero, A. Buts, S.I. Campbell, L. Chapon, et al., Mantis—Data analysis and visualization package for neutron scattering and SR experiments, nuclear instruments and methods in physics research section a: accelerators, spectrometers, *Detect. Assoc. Equip.* 764 (2014) 156–166, <http://dx.doi.org/10.1016/j.nima.2014.07.029>.
- [39] V. Bonnard, J.L. Chaboche, P. Gomez, P. Kanouté, D. Pacou, Investigation of multiaxial fatigue in the context of turboengine disc applications, *Int. J. Fatigue* 33 (2011) 1006–1016, <http://dx.doi.org/10.1016/j.ijfatigue.2010.12.018>.
- [40] R.A. Cláudio, L. Reis, M. Freitas, Biaxial high-cycle fatigue life assessment of ductile aluminium cruciform specimens, *Theor. Appl. Fract. Mech.* 73 (2014) 82–90, <http://dx.doi.org/10.1016/j.tafmec.2014.08.007>.
- [41] T. Lorentzen, M. Hutchings, P. Withers, T. Holden, *Introduction to the Characterization of Residual Stress by Neutron Diffraction*, CRC Press, 2005 (accessed 11.9 15.), <http://www.crcnetbase.com/doi/book/10.1201/9780203402818>.
- [42] Iso Standard ISO/TS 21432:(2005)(E): Non-destructive Testing – Standard Test Method for Determining Residual Stresses by Neutron Diffraction, 2005-07-15, International Organization for Standardization, Geneva, Switzerland, (n.d.).
- [43] Distortional Hardening Rules for Metal Plasticity, *J. Eng. Mech.* 109 (1983) 1042–1057, [http://dx.doi.org/10.1061/\(ASCE\)0733-9399\(1983\)109:4\(1042\)](http://dx.doi.org/10.1061/(ASCE)0733-9399(1983)109:4(1042)).
- [44] Z.H.C. Teodosiu, *Microstructure in the Continuum Modeling of Plastic Anisotropy, Modelling of Structure and Mechanics of Materials from Micro-scale to Products, 1998*.
- [45] I. Karaman, H. Sehitoglu, H.J. Maier, Y.I. Chumlyakov, Competing mechanisms and modeling of deformation in austenitic stainless steel single crystals with and without nitrogen, *Acta Mater.* 49 (2001) 3919–3933, [http://dx.doi.org/10.1016/S1359-6454\(01\)00296-8](http://dx.doi.org/10.1016/S1359-6454(01)00296-8).
- [46] F. Hamdi, S. Asgari, Evaluation of the role of deformation twinning in work hardening behavior of face-centered-cubic polycrystals, *Metall. Mater. Trans. A* 39 (2007) 294–303, <http://dx.doi.org/10.1007/s11661-007-9356-6>.
- [47] A. Borbély, J. Dragomir-Cernatescu, G. Ribárik, T. Ungár, Computer program ANIZC for the calculation of diffraction contrast factors of dislocations in elastically anisotropic cubic, hexagonal and trigonal crystals, *J. Appl. Cryst.* 36 (2003) 160–162, <http://dx.doi.org/10.1107/S0021889802021581>.
- [48] T. Ungár, Á. Révész, A. Borbély, Dislocations and grain size in electrodeposited nanocrystalline ni determined by the modified williamson–hall and warren–averbach procedures, *J. Appl. Cryst.* 31 (1998) 554–558, <http://dx.doi.org/10.1107/S0021889897019559>.
- [49] T. Ungár, Microstructural parameters from x-ray diffraction peak broadening, *Scr. Mater.* 51 (2004) 777–781, <http://dx.doi.org/10.1016/j.scriptamat.2004.05.007>.
- [50] E.J. Mittemeijer, U. Welzel, *Modern Diffraction Methods, Wiley-VCH, Weinheim, Germany, 2013*.
- [51] Y. Zhou, K.W. Neale, Texture evolution during the biaxial stretching of fcc sheet metals, *Textures Microstruct.* 22 (1993) 87–111, <http://dx.doi.org/10.1155/TSM.22.87>.
- [52] J.L. Chaboche, A review of some plasticity and viscoplasticity constitutive theories, *Int. J. of Plast.* 24 (2008) 1642–1693, <http://dx.doi.org/10.1016/j.ijplas.2008.03.009>.
- [53] N.A. Sakharova, M.M. Vieira, J.V. Fernandes, M.F. Vieira, Strain Path change effect on deformation behaviour of materials with low-to-moderate stacking fault energy, *Mater. Sci. Forum* 587–588 (2008) 420–424, <http://dx.doi.org/10.4028/www.scientific.net/MSF.587-588.420>.
- [54] L. Li, S. Van Petegem, H. Van Swygenhoven, P.M. Anderson, Slip-induced intergranular stress redistribution in nanocrystalline Ni, *Acta Mater.* 60 (2012) 7001–7010, <http://dx.doi.org/10.1016/j.actamat.2012.09.007>.